Partition of unity enrichment for bimaterial interface cracks

N. Sukumar[1,*,†], Z. Y. Huang[2,‡], J.-H. Prévost[3] and Z. Suo[2,‡]

[1]*Department of Civil and Environmental Engineering, University of California, One Shields Avenue, Davis, CA 95616, U.S.A.*
[2]*Department of Mechanical and Aerospace Engineering, Princeton University, NJ 08544, U.S.A.*
[3]*Department of Civil and Environmental Engineering, Princeton University, NJ 08544, U.S.A.*

SUMMARY

Partition of unity enrichment techniques are developed for bimaterial interface cracks. A discontinuous function and the two-dimensional near-tip asymptotic displacement functions are added to the finite element approximation using the framework of partition of unity. This enables the domain to be modelled by finite elements without explicitly meshing the crack surfaces. The crack-tip enrichment functions are chosen as those that span the asymptotic displacement fields for an interfacial crack. The concept of partition of unity facilitates the incorporation of the oscillatory nature of the singularity within a conforming finite element approximation. The mixed-mode (complex) stress intensity factors for bimaterial interfacial cracks are numerically evaluated using the domain form of the interaction integral. Good agreement between the numerical results and the reference solutions for benchmark interfacial crack problems is realized. Copyright © 2004 John Wiley & Sons, Ltd.

KEY WORDS: extended finite element method; interface crack; oscillatory singularity; stress intensity factor; four-point bending specimen; steady-state energy release rate

1. INTRODUCTION

With the increasing demands on multi-functional needs (wear, corrosion, thermal resistance and toughness) in mechanical, aerospace and biomedical applications, the development of multi-layered material systems has come to the forefront. The overall mechanical behaviour and response of layered systems hinges on the mechanical properties and fracture/fatigue behaviour of the interfaces. The presence of weak fibre–matrix interfaces in ceramic composites provide preferential crack paths that enhance the overall fracture toughness of the composite [1].

---

*Correspondence to: N. Sukumar, Department of Civil and Environmental Engineering, University of California, One Shields Avenue, Davis, CA 95616, U.S.A.
†E-mail: nsukumar@ucdavis.edu
‡Present address: Division of Engineering and Applied Sciences, Harvard University, Cambridge, MA 02138, U.S.A.

Debonding in adhesive joints, composite laminates and at film-substrate interfaces, crack growth along bimaterial interfaces and the structural integrity of thin films are a few examples that highlight the role of interfacial mechanics. A comprehensive review on mixed-mode cracking in layered systems is provided by Hutchinson and Suo [2]. The development of a robust simulation tool to characterize the crack driving force and interfacial toughness in bimaterial systems can lead to a better understanding of the role and influence of the mismatch in properties (elastic and thermal) and their effects on crack growth. To this end, in this paper we propose a partition of unity-based enrichment method for bimaterial interfacial cracks.

Fracture parameters such as the stress intensity factors (SIFs) or the energy release rate (crack driving force) are measures of the intensity of the crack-tip fields. Finite element and boundary element methods are the primary methods of choice in the numerical analysis of cracks in isotropic and bimaterial media. In linear elastic fracture mechanics, the stresses and strains are inverse square-root singular at the crack tip ($\sigma_{ij} \sim 1/\sqrt{r}$, $\varepsilon_{ij} \sim 1/\sqrt{r}$), where r is the radial distance from the crack tip. To model the $\sqrt{r}$-behaviour in displacement-based finite element computations, the eight-node quarter-point element as well as the six-node (collapsed quadrilateral) quarter-point element were introduced [3–5].

For cracks in bimaterial media, the problem of a crack normal (and impinging) to a bimaterial interface and that of an interface crack are of technological importance. For a bimaterial with a crack perpendicular to the interface, the near-tip stress field is of the form $\sigma_{ij} \sim r^{-\lambda}$ ($0 < \lambda < 1$) [6, 7], where the exponent λ is given by the solution of a transcendental equation [6] and is dependent on the Dundurs parameters [8]. To model this behaviour within finite elements, efforts have been made to embed arbitrary-order singularities ($r^{-\lambda}$, $0 < \lambda < 1$) in the vicinity of the crack tip [9–14]; however, most of these approaches require significant changes in existing finite element codes. Abdi and Valentin [15] generalized the idea of quarter-point elements for modelling an $r^{-\lambda}$ stress-singularity, and improvements on this technique with respect to the optimal positioning of nodes have been recently proposed [16, 17]. In Reference [18], a review on special finite elements (including stress hybrid singular elements) for plane crack problems is presented.

The theoretical foundations for bimaterial interface cracks was pioneered by Williams [19], and further extended by Rice and Sih [20]. Rice [21] clarified the interpretation of the complex stress intensity factor as well as unified some of the earlier developments on interfacial crack mechanics, and the notations and definitions in Reference [21] are now universally adopted in the exposition of linear elastic interfacial fracture mechanics. Notably, a complex **K** for bimaterial interfacial cracks was proposed that reduced to the classical definition (K_{I}, K_{II}) in the absence of any mismatch in material properties ($\varepsilon = 0$). The stress singularity in the vicinity of the crack tip of a bimaterial interface crack is oscillatory in nature, along with the presence of an inverse $\sqrt{r}$-singularity, i.e. $\sigma_{22} + \mathrm{i}\tau_{12} \sim r^{-1/2}\mathrm{e}^{\mathrm{i}\varepsilon \log r}$ [19]. The oscillatory singularity introduces significant complexity in an element formulation, and hence the incorporation of the full radial dependence of the crack-tip displacement field has not been pursued within a classical finite element framework. Typically, non-singular isoparametric finite elements are used in interfacial fracture computations [22–26]. In References [23, 25], the domain form of the contour interaction integral [22, 27] was used to extract the stress intensity factors. Matos *et al.* [24] applied the virtual crack extension method, whereas Bjerkén and Persson [26] adopted the crack closure integrals to evaluate the SIFs.

In this paper, we develop a partition of unity-based enrichment method for bimaterial interfacial cracks. This work extends the capabilities of the extended finite element method (X-FEM)

[28–31] to the analysis of cracks that lie at the interface of two elastically homogeneous isotropic materials. A detailed description of the numerical implementation of the X-FEM for 2D crack modelling in isotropic media and for a crack normal to a bimaterial interface is given in Reference [32], whereas in Reference [33], applications of the method for quasi-static crack growth simulations are presented. In this study, interfacial crack modelling within the X-FEM framework is proposed, and a numerical study of the accuracy and robustness of the method is conducted. The numerical implementation is carried out within $\texttt{Dynaflow}^{TM}$ [34]. In Section 2, the main ingredients of linear elastic interfacial fracture mechanics are summarized. In Section 3, we introduce the partition of unity method, and in Section 4, the extended finite element is presented. The modelling of bimaterial interfacial cracks is described in Section 4.1, and domain integral methods for interfacial cracks are discussed in Section 5. The weak form and discrete equations for the bimaterial interface crack problem are given in Section 6. Numerical results for benchmark interfacial crack problems are presented in Section 7, and a few concluding remarks are mentioned in Section 8.

2. INTERFACIAL FRACTURE MECHANICS

Consider the schematic of a bimaterial interface crack shown in Figure 1. The crack is located along the interface that is between two semi-infinite planes. Let the plane above the crack be denoted by material 1 with Young's modulus and Poisson's ratio of E_1 and ν_1, respectively,
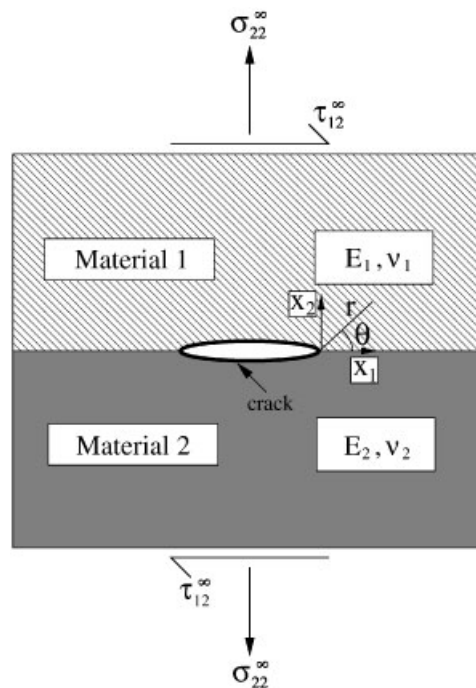

Figure 1. Bimaterial interface crack.

and let the plane below the crack be material 2 with corresponding properties of E_2 and v_2. We proceed to summarize some of the essential ingredients of linear elastic interfacial fracture mechanics [21, 35, 36].

Let $\mathbf{K} = K_1 + iK_2$ be the complex stress intensity factor. The in-plane traction vector at a distance r ahead of the crack takes the form [19]

$$(\sigma_{22} + i\tau_{12})_{\theta=0} = \frac{\mathbf{K}r^{i\varepsilon}}{\sqrt{2\pi r}} \tag{1}$$

where $i = \sqrt{-1}$, and ε is the bimaterial constant that is defined in Equation (6b). From the above equation, we note that the dimension of $\mathbf{K}$ is [stress][length]$^{1/2-i\varepsilon}$, whereas that of its amplitude $|\mathbf{K}|$ is the familiar [stress][length]$^{1/2}$. The energy release rate can be related to the stress intensity factor amplitude through the relation [37]

$$\mathcal{G} = \frac{1}{E^*} \frac{|\mathbf{K}|^2}{\cosh^2(\pi\varepsilon)}, \quad |\mathbf{K}|^2 = \mathbf{K}\bar{\mathbf{K}} = K_1^2 + K_2^2 \tag{2a}$$

where

$$\frac{2}{E^*} = \frac{1}{\bar{E}_1} + \frac{1}{\bar{E}_2}, \quad \bar{E}_i = \begin{cases} E_i & \text{(plane stress)} \\ \dfrac{E_i}{1 - v_i^2} & \text{(plane strain)} \end{cases} \quad (i = 1, 2) \tag{2b}$$

The phase angle ψ is a measure of the relative proportion of shear to normal tractions at a characteristic distance ℓ ahead of the crack tip. It is defined through the relation [21]

$$\mathbf{K}\ell^{i\varepsilon} = |\mathbf{K}|e^{i\psi} \tag{3}$$

or

$$\psi = \tan^{-1}\left(\frac{\text{Im}[\mathbf{K}\ell^{i\varepsilon}]}{\text{Re}[\mathbf{K}\ell^{i\varepsilon}]}\right) \tag{4}$$

The phase angle ψ is an important parameter in the characterization of interfacial fracture toughness. In reporting the phase angle for a given loading configuration, the characteristic length ℓ is taken as the crack (ligament) length or a specimen dimension. It is apparent from the above discussion that, unlike the treatment of cracks in isotropic media, tension and shear effects are inseparable in the vicinity of interface crack tips and as a consequence K_1 and K_2 are not the familiar mode I and mode II stress intensity factors, respectively.

The Cartesian components of the near-tip asymptotic displacement fields can be obtained from Reference [21]. The crack-tip displacement fields in the upper-half plane (replace $\varepsilon\pi$ by $-\varepsilon\pi$ for the lower-half plane) are [38]

$$u_j = \frac{1}{2\mu_1}\sqrt{\frac{r}{2\pi}}\{\text{Re}[\mathbf{K}r^{i\varepsilon}]\tilde{u}_j^{\text{I}}(\theta, \varepsilon, v_1) + \text{Im}[\mathbf{K}r^{i\varepsilon}]\tilde{u}_j^{\text{II}}(\theta, \varepsilon, v_1)\} \quad (j = 1, 2) \tag{5a}$$

$$\tilde{u}_1^{\text{I}} = A\left[-e^{2\varepsilon(\pi-\theta)}\left(\cos\frac{\theta}{2} + 2\varepsilon\sin\frac{\theta}{2}\right) + \kappa_1\left(\cos\frac{\theta}{2} - 2\varepsilon\sin\frac{\theta}{2}\right) + (1 + 4\varepsilon^2)\sin\frac{\theta}{2}\sin\theta\right] \tag{5b}$$

Figure 2. Angular functions in the asymptotic displacement field: (a) $\tilde{u}_1^{\mathrm{I}}$, $\tilde{u}_1^{\mathrm{II}}$; and (b) $\tilde{u}_2^{\mathrm{I}}$, $\tilde{u}_2^{\mathrm{II}}$.

$$\tilde{u}_1^{\mathrm{II}} = A \left[\mathrm{e}^{2\varepsilon(\pi-\theta)} \left(\sin\frac{\theta}{2} - 2\varepsilon \cos\frac{\theta}{2} \right) + \kappa_1 \left(\sin\frac{\theta}{2} + 2\varepsilon \cos\frac{\theta}{2} \right) + (1+4\varepsilon^2) \cos\frac{\theta}{2} \sin\theta \right]$$

(5c)

$$\tilde{u}_2^{\mathrm{I}} = A \left[\mathrm{e}^{2\varepsilon(\pi-\theta)} \left(\sin\frac{\theta}{2} - 2\varepsilon \cos\frac{\theta}{2} \right) + \kappa_1 \left(\sin\frac{\theta}{2} + 2\varepsilon \cos\frac{\theta}{2} \right) - (1+4\varepsilon^2) \cos\frac{\theta}{2} \sin\theta \right]$$

(5d)

$$\tilde{u}_2^{\mathrm{II}} = A \left[\mathrm{e}^{2\varepsilon(\pi-\theta)} \left(\cos\frac{\theta}{2} + 2\varepsilon \sin\frac{\theta}{2} \right) - \kappa_1 \left(\cos\frac{\theta}{2} - 2\varepsilon \sin\frac{\theta}{2} \right) + (1+4\varepsilon^2) \sin\frac{\theta}{2} \sin\theta \right]$$

(5e)

where

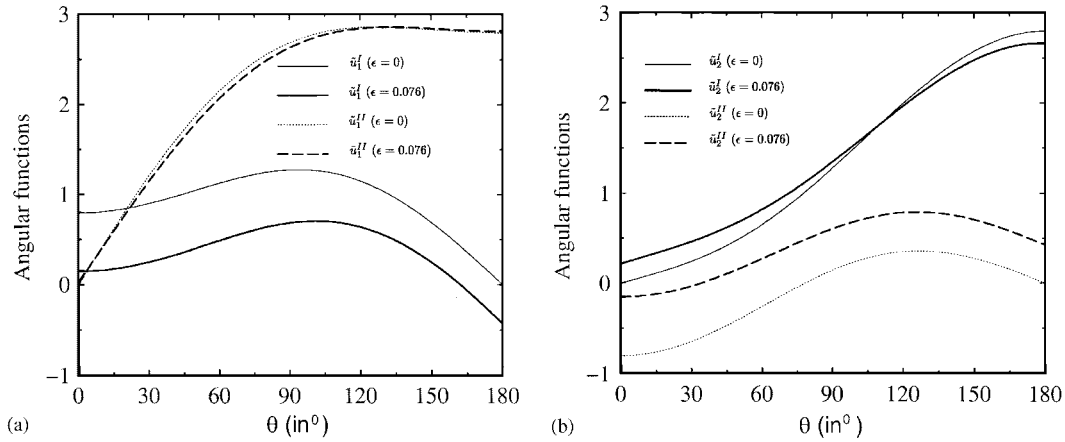$$A = \frac{\mathrm{e}^{-\varepsilon(\pi-\theta)}}{(1+4\varepsilon^2)\cosh(\pi\varepsilon)}$$

and (r, θ) are polar co-ordinates with origin at the right crack tip.

The angular functions in Equation (5) are plotted in Figure 2 for $\varepsilon = 0$ (no mismatch) and $\varepsilon = 0.076$ ($E_1/E_2 = 0.1$, $\nu_1 = \nu_2 = 0.3$). Plane strain conditions are assumed. In Equation (5a), $\mathrm{Re}[\cdot]$ and $\mathrm{Im}[\cdot]$ denote the real and imaginary parts of a complex number, and $r^{\mathrm{i}\varepsilon} = \mathrm{e}^{\mathrm{i}\varepsilon \log r} = \cos(\varepsilon \log r) + \mathrm{i}\sin(\varepsilon \log r)$. In addition, ε is the bimaterial constant which is a function of β, the second Dundurs parameter [8]:

$$\alpha = \frac{\mu_1(\kappa_2+1) - \mu_2(\kappa_1+1)}{\mu_1(\kappa_2+1) + \mu_2(\kappa_1+1)}, \quad \beta = \frac{\mu_1(\kappa_2-1) - \mu_2(\kappa_1-1)}{\mu_1(\kappa_2+1) + \mu_2(\kappa_1+1)}$$

(6a)

$$\varepsilon = \frac{1}{2\pi} \log\left(\frac{1-\beta}{1+\beta}\right) \tag{6b}$$

$$\kappa_i = \begin{cases} \dfrac{3-v_i}{1+v_i} & \text{(plane stress)} \\[2mm] 3-4v_i & \text{(plane strain)} \end{cases} \tag{6c}$$

where μ_i, v_i and κ_i are the shear modulus, Poisson's ratio and the Kolosov constant, respectively, of material i $(i = 1, 2)$.

3. PARTITION OF UNITY METHOD

The partition of unity finite element method [39] is a generalization of the standard Galerkin finite element method. In the literature, numerical techniques such as the X-FEM [29, 30], generalized finite element method (GFEM) [40], or the element partition method [41] are all particular instances of the partition of unity method. In finite elements, a basis function N_I is associated with node I in the mesh. Let ω_I denote the region of support for N_I: $\omega_I = \{\mathbf{x} : N_I(\mathbf{x}) > 0\}$. The nodes belonging to an element are given by the connectivity of the element, whereas its dual ω_I, is the collection of elements that are associated with a specific node I. The partition of unity approximation for a scalar-valued function u can be written in the general form [39]:

$$u^h(\mathbf{x}) = \sum_{I=1}^{N} N_I(\mathbf{x}) \left(\sum_{\alpha=1}^{M} \psi_\alpha(\mathbf{x}) a_I^\alpha \right) \tag{7}$$

where ψ_J are enrichment functions, and a_I^α are unknown coefficients that are associated with: (1) node I; (2) the enrichment function ψ_α; and (3) a specific geometric entity (such as a crack). The finite element shape functions form a partition of unity: $\sum_I N_I(\mathbf{x}) = 1$. From Equation (7), we note that the classical finite element space ($\psi_1 \equiv 1$; $\psi_\alpha = 0$ $(\alpha \neq 1)$) is a sub-space of the enriched space. Since the enrichment function ψ_α is multiplied by the basis function N_I, the product $N_I \psi_\alpha$ has compact support. A standard Galerkin procedure is used to obtain the discrete equations, and the symmetry and sparsity of the stiffness matrix are also retained.

Even though the idea of augmenting the classical finite element approximation by known asymptotic solutions is not new [10, 42, 43], unlike previous attempts in this direction, the partition of unity framework satisfies a few key properties that renders it a powerful tool for local enrichment within a finite element setting:

1. can include application-specific basis functions to better approximate the solution;
2. automatic enforcement of continuity (conforming trial-and-test approximations); and
3. point or line singularities as well as surface discontinuities can be handled without the need for the discontinuous surfaces to be aligned with the finite element mesh.

The above properties provide a means to include and represent any function through the finite element approximation. This is in contrast to enriched finite elements [10, 12], where transition elements are required to satisfy displacement continuity. On using the partition of unity approximation in linear elasticity, the ability to represent rigid-body translation and

constant-strain modes (sufficient condition for convergence of second-order partial differential equations) is retained; however, in Reference [11] where power-type singularities are introduced, constant-strain (and rigid rotations) terms cannot be represented and hence apart from convergence issues, these elements are also unsuitable for thermal stress problems.

4. EXTENDED FINITE ELEMENT METHOD

The ability to model crack discontinuities within finite elements by enriching the classical finite element displacement approximation is a recent development in computational fracture mechanics [28, 29]. The numerical technique was coined as the X-FEM [30]. In the X-FEM, the emphasis has been on modelling discontinuities (such as cracks) with minimal enrichment. For crack modelling in isotropic linear elasticity, a discontinuous function and the two-dimensional asymptotic crack-tip displacement fields are used to account for the crack. This enables the domain to be modelled by finite elements without explicitly meshing the crack surfaces, and hence quasi-static or fatigue crack propagation simulations can be carried out without remeshing. The concept of partition of unity [39] enables the incorporation of different types of singularities (cracks in isotropic and bimaterial media). The near-tip solution for a crack normal to a bimaterial interface was introduced in Reference [44], and in this paper, the asymptotic near-tip fields for an interfacial crack are used. We first describe some of the essential concepts related to 2D crack modelling in isotropic media [29], and then discuss the specifics related to bimaterial interface crack modelling.

Consider a single crack in two dimensions. Let Γ_c be the crack surface (interior) and Λ_c the crack tip—the closure $\bar{\Gamma}_c = \Gamma_c \cup \Lambda_c$. The enriched displacement (trial and test) approximation for 2D crack modelling is of the form [29]:

$$\mathbf{u}^h(\mathbf{x}) = \sum_{I \in \mathcal{N}} N_I(\mathbf{x}) \left[\mathbf{u}_I + \underbrace{H(\mathbf{x})\mathbf{a}_I}_{I \in \mathcal{N}_\Gamma} + \underbrace{\sum_{\alpha=1}^{4} \Phi_\alpha(\mathbf{x})\mathbf{b}_I^\alpha}_{I \in \mathcal{N}_\Lambda} \right] \tag{8}$$

where $\mathbf{u}_I$ is the nodal displacement vector associated with the continuous part of the finite element solution, $\mathbf{a}_I$ is the nodal enriched degree-of-freedom vector associated with the Heaviside function (assumes the value $+1$ above the crack and -1 below the crack), and $\mathbf{b}_I^\alpha$ is the nodal enriched degree-of-freedom vector associated with the elastic asymptotic crack-tip functions. In the above equation, $\mathcal{N}$ is the set of all nodes in the mesh; $\mathcal{N}_\Gamma$ is the set of nodes whose shape function support is cut by the crack interior Γ_c; and $\mathcal{N}_\Lambda$ is the set of nodes whose shape function support is cut by the crack tip Λ_c ($\mathcal{N}_\Gamma \cap \mathcal{N}_\Lambda = \emptyset$):

$$\mathcal{N}_\Lambda = \{n_K : n_K \in \mathcal{N}, \bar{\omega}_K \cap \Lambda_c \neq \emptyset\} \tag{9}$$

$$\mathcal{N}_\Gamma = \{n_J : n_J \in \mathcal{N}, \omega_J \cap \Gamma_c \neq \emptyset, n_J \notin \mathcal{N}_\Lambda\} \tag{10}$$

For further details on the implementation of the X-FEM, the interested reader can refer to References [29, 32].

4.1. Bimaterial interface crack modelling

To model interface cracks within the X-FEM setting, we use the generalized Heaviside functions $H(\mathbf{x})$ to model the crack interior (Γ_c), and the asymptotic crack-tip functions $[\Phi_\alpha(\mathbf{x}), \alpha = 1\text{--}12]$ to model the crack tip (Λ_c) for an interface crack. From Equation (5), we can write the near-tip crack enrichment functions for a bimaterial interfacial crack as

$$[\Phi_\alpha(\mathbf{x}), \alpha = 1\text{--}12] = \left\{ \sqrt{r}\,\cos(\varepsilon \log r)\mathrm{e}^{-\varepsilon\theta}\,\sin\frac{\theta}{2}, \sqrt{r}\,\cos(\varepsilon \log r)\mathrm{e}^{-\varepsilon\theta}\,\cos\frac{\theta}{2} \right.$$

$$\sqrt{r}\,\cos(\varepsilon \log r)\mathrm{e}^{\varepsilon\theta}\,\sin\frac{\theta}{2}, \sqrt{r}\,\cos(\varepsilon \log r)\mathrm{e}^{\varepsilon\theta}\,\cos\frac{\theta}{2}$$

$$\sqrt{r}\,\cos(\varepsilon \log r)\mathrm{e}^{\varepsilon\theta}\,\sin\frac{\theta}{2}\,\sin\theta, \sqrt{r}\,\cos(\varepsilon \log r)\mathrm{e}^{\varepsilon\theta}\,\cos\frac{\theta}{2}\,\sin\theta$$

$$\sqrt{r}\,\sin(\varepsilon \log r)\mathrm{e}^{-\varepsilon\theta}\,\sin\frac{\theta}{2}, \sqrt{r}\,\sin(\varepsilon \log r)\mathrm{e}^{-\varepsilon\theta}\,\cos\frac{\theta}{2}$$

$$\sqrt{r}\,\sin(\varepsilon \log r)\mathrm{e}^{\varepsilon\theta}\,\sin\frac{\theta}{2}, \sqrt{r}\,\sin(\varepsilon \log r)\mathrm{e}^{\varepsilon\theta}\,\cos\frac{\theta}{2}$$

$$\left. \sqrt{r}\,\sin(\varepsilon \log r)\mathrm{e}^{\varepsilon\theta}\,\sin\frac{\theta}{2}\,\sin\theta, \sqrt{r}\,\sin(\varepsilon \log r)\mathrm{e}^{\varepsilon\theta}\,\cos\frac{\theta}{2}\,\sin\theta \right\} \quad (11)$$

where r and θ are polar co-ordinates in the local crack-tip co-ordinate system. The above functions span the near-tip displacement field given in Equation (5). The Cartesian derivatives of the enrichment functions are listed in Appendix A.

If the bimaterial constant $\varepsilon = 0$ (isotropic material), the span of the enrichment functions given in Equation (11) is

$$[\Phi_\alpha(\mathbf{x}), \alpha = 1\text{--}4] = \left[\sqrt{r}\,\sin\frac{\theta}{2}, \sqrt{r}\,\cos\frac{\theta}{2}, \sqrt{r}\,\sin\frac{\theta}{2}\,\sin\theta, \sqrt{r}\,\cos\frac{\theta}{2}\,\sin\theta \right] \quad (12)$$

which are the near-tip enrichment functions used in Equation (8) to model a crack in isotropic media [28, 29].

The enriched nodes for a bimaterial interface crack (Γ_c) are shown in Figure 3. The nodes that are shown by open circles are enriched by the Heaviside function, whereas the ones with the filled circles are enriched with the near-tip functions. Since the edges of the finite element coincide with the interface Γ, all the nodes that are enriched by the Heaviside function lie on the crack surface; if the other nodes that belong to the same element and which lie in Ω_1 or Ω_2 are also enriched, then linear dependencies will arise that will lead to the presence of spurious singular modes in the linear system of equations (singular stiffness matrix). Issues pertaining to linear dependencies for arbitrarily oriented cracks are discussed in Reference [29].

In the modelling of cracks that have arbitrary orientation with respect to the finite elements, partitioning algorithms are required [29, 30]; detailed discussion on the theoretical need for element partitioning and its distinction from *de facto* remeshing is provided in Reference [32].
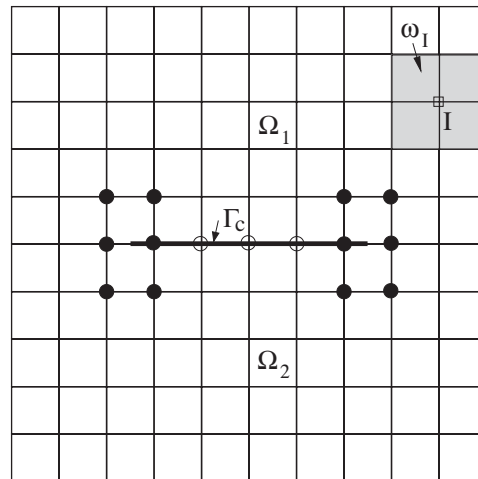
Figure 3. Enriched nodes for a bimaterial interface crack. The nodes enriched with the Heaviside function are shown by open circles, and the nodes enriched with the near-tip asymptotic functions are shown by filled circles. The shaded region is the nodal shape function support ω_I.

In the present instance, since the interface crack is coincident with element edges, no element partitioning is needed. Accuracy considerations in the numerical integration of the weak form, however, do necessitate the use of higher-order Gauss quadrature rules in elements with enriched degrees of freedom. We decompose such elements into triangles (near-tip enriched elements are each split into two triangles) and use a 12-point rule in each sub-triangle. In numerical tests, the use of a six-point rule lead to a nearly singular (ill-conditioned) stiffness matrix. A 12-point rule was sufficient to obtain a well-conditioned matrix for the accurate solution of the discrete system.

5. DOMAIN INTEGRAL METHODS FOR INTERFACIAL CRACKS

The general two-dimensional crack-tip contour integral can be written as [45]

$$L = \lim_{\Gamma \to 0} \int_{\Gamma} P_{1j} n_j \, d\Gamma \tag{13}$$

where Γ is a contour from the lower crack surface to the upper crack surface, and which encloses the crack tip. When the above integral pertains to the energy release rate due to unit crack extension in the plane, then $P_{1j} = W\delta_{1j} - \sigma_{ij} u_{i,1}$ (W is the strain energy density) which is the first component of Eshelby's energy-momentum tensor [46], and the above equation is then identical to Rice's path-independent J-integral:

$$J = \mathcal{G} = \int_{\Gamma} (W\delta_{1j} - \sigma_{ij} u_{i,1}) n_j \, d\Gamma \tag{14}$$

The J-integral remains globally path independent for bimaterial interface crack problems when there exists no material inhomogeneity in the direction parallel to the crack [47] (see Figure 1).
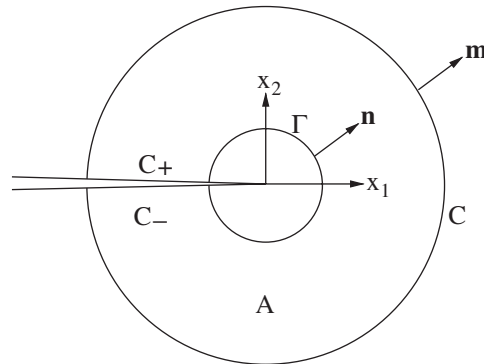
Figure 4. Domain integral representation. Domain A is enclosed by Γ, C_+, C_- and C.

In this case, the mixed-mode stress intensity factors K_1 and K_2 can be readily evaluated using the domain form [45, 48] of the contour interaction integral [22, 23].

In the interaction integral method [22, 27], the two-dimensional auxiliary fields are introduced and superposed on the actual fields that arise from the solution of the boundary-value problem. By judicious choice of the auxiliary fields, the interaction integral can be directly related to the stress intensity factors. On setting $P_{1j} = \sigma_{ik}\varepsilon_{ik}^{\mathrm{aux}}\delta_{1j} - \sigma_{ij}u_{i,1}^{\mathrm{aux}} - \sigma_{ij}^{\mathrm{aux}}u_{i,1}$ in Equation (13), we obtain the contour interaction energy integral [27]:

$$I = \int_{\Gamma} (\sigma_{ik}\varepsilon_{ik}^{\mathrm{aux}}\delta_{1j} - \sigma_{ij}u_{i,1}^{\mathrm{aux}} - \sigma_{ij}^{\mathrm{aux}}u_{i,1})n_j \, \mathrm{d}\Gamma \tag{15}$$

where u_i^{aux}, $\varepsilon_{ij}^{\mathrm{aux}}$ and $\sigma_{ij}^{\mathrm{aux}}$ are the auxiliary displacement, strain and stress fields, respectively. The interaction integral is related to the SIFs through the relation [27]

$$I = \frac{2}{E^* \cosh^2(\pi\varepsilon)} \left[K_1 K_1^{\mathrm{aux}} + K_2 K_2^{\mathrm{aux}} \right] \tag{16}$$

where K_1^{aux} and K_2^{aux} are local auxiliary stress intensity factors for the auxiliary fields, and E^* is defined in Equation (2b). On selecting $K_1^{\mathrm{aux}} = 1$ and $K_2^{\mathrm{aux}} = 0$ and evaluating $I = I_1$ (say), we can compute K_1 and we proceed in an analogous manner to evaluate K_2:

$$K_1 = \frac{E^* \cosh^2(\pi\varepsilon)}{2} I_1, \quad K_2 = \frac{E^* \cosh^2(\pi\varepsilon)}{2} I_2 \tag{17}$$

The domain form of the interaction integral is a well-established technique to determine the mixed-mode SIFs in 2D interfacial fracture computations [23, 25]. The domain form of the contour interaction integral in Equation (15) is [45]

$$I = -\int_{A} (\sigma_{ik}\varepsilon_{ik}^{\mathrm{aux}}\delta_{1j} - \sigma_{ij}u_{i,1}^{\mathrm{aux}} - \sigma_{ij}^{\mathrm{aux}}u_{i,1})q_{,j} \, \mathrm{d}A \tag{18}$$

where q is an arbitrarily smooth scalar weighting function that is unity at the crack tip and zero on the contour C (Figure 4). The auxiliary displacement fields for an interfacial crack can be extracted from Equation (5). In the implementation of the domain integral method,

we have used the expressions for the auxiliary fields that are provided in Reference [24]. For completeness, we have reproduced the fields in Appendix B, with a few additional details.

The domain integral in Equation (18) is evaluated using the X-FEM, and K_1 and K_2 are computed from Equation (17). The steps involved in the extraction of the SIFs follow. Finite elements that are within a radius of $r_d = r_k h_e$ from the crack-tip are selected. Here, h_e is the crack-tip element size and r_k is a user-specified scalar multiple [32]. All elements within a radius of r_d from the crack-tip are marked. Let us denote this element set by $\mathcal{N}_e^d$, with Ω_d^h defining the resulting discrete (union of elements) domain. The weighting function q that appears in the domain form of the interaction integral is then set: if a node n_i that is contained in the connectivity of element $e \in \mathcal{N}_e^d$ lies on the boundary $\partial\Omega_d^h$, then $q_i = 0$; if node n_i lies in Ω_d^h, then $q_i = 1$. Since the gradient of q appears in Equation (18), non-zero contribution to the integral is obtained only for elements with an edge that lie on $\partial\Omega_d^h$.

6. WEAK FORM AND DISCRETE EQUATIONS

Consider a bimaterial that consists of two materials labelled as 1 and 2 with domains Ω_1 and Ω_2, respectively (Figure 1). The problem domain $\Omega = \Omega_1 \cup \Omega_2$, and $\Gamma = \Omega_1 \cap \Omega_2$ is the interface. We assume that a crack Γ_c occupies part of Γ. In the absence of body forces, the weak form (principle of virtual work) for the discrete problem is

$$\int_{\Omega^h} \boldsymbol{\sigma} : \delta\boldsymbol{\varepsilon}^h \, d\Omega = \int_{\partial\Omega_t^h} \bar{\mathbf{t}} \cdot \delta\mathbf{u}^h \, d\Gamma \quad \forall \delta\mathbf{u}^h \in \mathbf{U}_0^h \tag{19}$$

where $\mathbf{u}^h(\mathbf{x}) \in \mathbf{U}^h$ and $\delta\mathbf{u}^h(\mathbf{x}) \in \mathbf{U}_0^h$ are the approximating trial-and-test functions, $\boldsymbol{\varepsilon}^h = \mathbf{u}_{()}^h$ is the small strain tensor, $\boldsymbol{\sigma}$ is the Cauchy stress tensor and δ is the first variation operator. In addition, $\boldsymbol{\sigma} = \mathbf{D} : \boldsymbol{\varepsilon}$ is the linear elastic constitutive relation, where $\mathbf{D}$ is the constitutive matrix (plane stress or plane strain) for material 1 or 2, and $\bar{\mathbf{t}}$ is the prescribed tractions. We point out that the X-FEM discrete spaces $\mathbf{U}^h$ and $\mathbf{U}_0^h$ contain functions that are discontinuous across the crack Γ_c. Following Equation (8), the approximating trial-and-test functions used to model bimaterial interface cracks are written in the form

$$\mathbf{u}^h(\mathbf{x}) = \sum_{I \in \mathcal{N}} N_I(\mathbf{x}) \left[\mathbf{u}_I + \underbrace{H(\mathbf{x})\mathbf{a}_I}_{I \in \mathcal{N}_\Gamma} + \underbrace{\sum_{\alpha=1}^{12} \Phi_\alpha(\mathbf{x})\mathbf{b}_I^\alpha}_{I \in \mathcal{N}_\Lambda} \right] \tag{20a}$$

$$\delta\mathbf{u}^h(\mathbf{x}) = \sum_{I \in \mathcal{N}} N_I(\mathbf{x}) \left[\mathbf{v}_I + \underbrace{H(\mathbf{x})\mathbf{c}_I}_{I \in \mathcal{N}_\Gamma} + \underbrace{\sum_{\alpha=1}^{12} \Phi_\alpha(\mathbf{x})\mathbf{e}_I^\alpha}_{I \in \mathcal{N}_\Lambda} \right] \tag{20b}$$

where the near-tip enrichment functions Φ_α are given in Equation (11). On substituting the above trial-and-test functions in Equation (19), and using the arbitrariness of nodal variations, the following discrete system of linear equations is obtained:

$$\mathbf{Kd} = \mathbf{f} \tag{21}$$

where $\mathbf{d}$ is the vector of nodal unknowns, and $\mathbf{K}$ and $\mathbf{f}$ are the global stiffness matrix and external force vector, respectively. For details on the specific forms of $\mathbf{K}$ and $\mathbf{f}$, see References [29, 32].

In the X-FEM, the traction-free conditions on the crack faces are satisfied in a weak (distributional) sense [28]. For a bimaterial, additional conditions need to be met along $\Gamma - \Gamma_c$: $[\![\mathbf{u}]\!] = \mathbf{0}$ and $[\![\boldsymbol{\sigma} \cdot \mathbf{n}]\!] = \mathbf{0}$, where $[\![\cdot]\!]$ denotes a jump in the indicated quantity. The first condition (displacement continuity) is automatically satisfied since the X-FEM trial function is continuous across $\Gamma - \Gamma_c$. The second condition, namely traction continuity at the material interface is met weakly since the edges of the finite elements are aligned with Γ. We point out that the alignment of the finite element mesh with the interface is not a restriction of the method; enrichment of the displacement field (normal strain is discontinuous across the interface) for material interface problems has been developed where the interface need not coincide with the edges of the finite element [49].

7. NUMERICAL RESULTS

We present numerical results for three benchmark problems. First, the accuracy of the SIFs and the convergence of the numerical method is studied when the exact near-tip displacement field is imposed on the boundary of a bimaterial plate that contains a crack that extends from the perimeter to the centre of the specimen. Secondly, we consider the problem of a centre-crack in an infinite bimaterial plate and compare the numerical results for the SIFs to the exact solution [20, 21] for both, pure tension and pure shear far-field loading. As the third problem, we consider the bimaterial, notched four-point bending specimen and compare the steady-state energy release rate to the analytical solution obtained by Charalambides *et al.* [50]. In all the numerical examples, the SIFs and the energy release rate are computed using the domain form of the contour interaction integral (see Section 5).

7.1. Convergence study

Consider a bimaterial plate of dimensions $(-L, L) \times (-L, L)$ with a crack of length L that extends from $(-L, 0)$ to $(0, 0)$. Using Equation (5), we impose the near-tip displacement field corresponding to $K_1 = 1$ and $K_2 = 1$ on the boundary of the specimen. The material properties chosen are: $E_1 = 10$, $E_2 = 1$, $v_1 = v_2 = 0.3$. To test the implementation and the rate of convergence of the proposed technique, two different specimen dimensions are selected ($L = 1$ and $L = 10$). The SIFs and the relative error in the energy norm are computed as the mesh is refined (h_e is the mesh spacing). The exact energy norm and the error in the energy norm are defined as

$$\|\mathbf{u}\|_{E(\Omega)} = \left(\frac{1}{2} \int_\Omega \boldsymbol{\varepsilon}^{\mathrm{T}} \mathbf{D} \boldsymbol{\varepsilon} \, \mathrm{d}\Omega \right)^{1/2}, \quad \|\mathbf{u} - \mathbf{u}^h\|_{E(\Omega)} = \left(\frac{1}{2} \int_\Omega (\boldsymbol{\varepsilon} - \boldsymbol{\varepsilon}^h)^{\mathrm{T}} \mathbf{D} (\boldsymbol{\varepsilon} - \boldsymbol{\varepsilon}^h) \, \mathrm{d}\Omega \right)^{1/2} \tag{22}$$
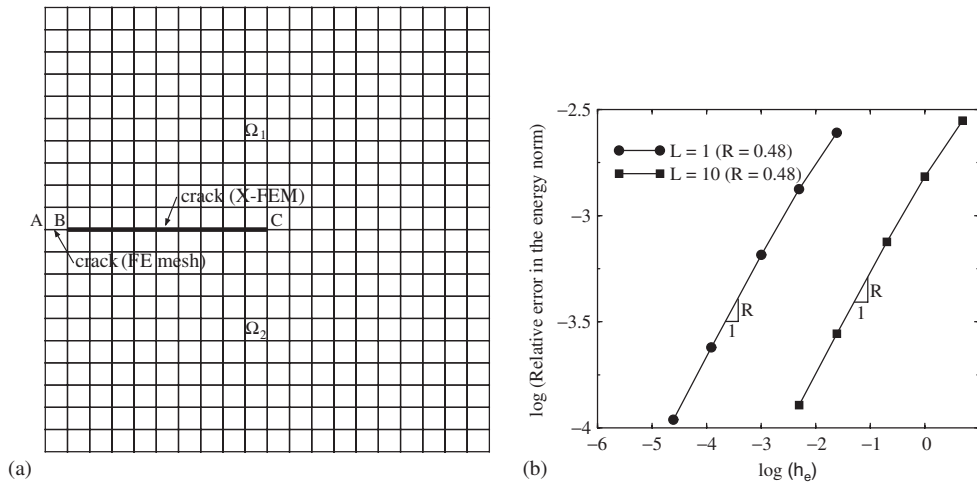
Figure 5. Convergence study: (a) mesh (20×20); and (b) rate of convergence in the energy norm.

Five different meshes are considered: 10×10, 20×20, 40×40, 100×100 and 200×200; a sample mesh (20×20 elements) is shown in Figure 5(a). To impose the essential boundary conditions, the crack is explicitly meshed over one element (AB), whereas the remaining part of the crack (BC) is modelled by the X-FEM (see Figure 5(a)). The scaling factor $r_k = 4$ is used in the domain integral computations. The results of the convergence study are listed in Table I. The numerical computations are carried out with near-tip and Heaviside enrichment functions, and also with just the Heaviside function as an enrichment function. The discrete space in the latter case is identical to that obtained with finite elements. In Figure 5(b), the relative error in the energy norm for the X-FEM (near-tip and Heaviside enrichment) is plotted as a function of the mesh spacing h_e (log–log plot); the rate of convergence R is also indicated. A rate of *one-half* is realized, which matches the theoretical convergence rate of the finite element method in the presence of a dominant $\sqrt{r}$-singularity [43]. The use of the near-tip fields in only a few elements is not sufficient to increase the overall rate of convergence of the method; however, the incorporation of the asymptotic fields into the displacement approximation improves the accuracy *vis-à-vis* the finite element method.

7.2. Centre-crack in an infinite bimaterial plate

We consider the problem of an interfacial crack located in between two dissimilar elastic semi-infinite planes (Figure 1). The exact solution to this problem under remote traction $\mathbf{t} = \sigma_{22}^\infty + i\tau_{12}^\infty$ was obtained by Rice and Sih [20]. The solution for K_1 and K_2 at the right crack tip is [20, 21]:

$$\mathbf{K} = K_1 + iK_2 = (\sigma_{22}^\infty + i\tau_{12}^\infty)(1 + 2i\varepsilon)\sqrt{\pi a}(2a)^{-i\varepsilon} \qquad (23)$$

An in-depth numerical investigation is conducted, with the following objectives:

- to study domain independence and the influence of the element size on the SIFs;
- robustness study: accuracy of the SIFs under small perturbations of the crack-tip;
- explore finite size specimen effects and trends in the SIFs;

Table I. Convergence study: stress intensity factors and
relative error in the energy norm.

Domain (Enrichment)	Mesh (h_e)	K_1	K_2	$\dfrac{\|\mathbf{u}-\mathbf{u}^h\|_{E(\Omega)}}{\|\mathbf{u}\|_{E(\Omega)}}$
2×2	10×10 (0.20)	1.0003	0.9989	7.353×10^{-2}
(Φ_α and H)	20×20 (0.10)	1.0005	0.9995	5.641×10^{-2}
	40×40 (0.05)	1.0005	0.9994	4.140×10^{-2}
	100×100 (0.02)	1.0007	0.9994	2.676×10^{-2}
	200×200 (0.01)	1.0008	0.9994	1.905×10^{-2}
2×2	10×10 (0.20)	1.0463	1.0415	2.180×10^{-1}
(H)	20×20 (0.10)	1.0240	1.0202	1.549×10^{-1}
	40×40 (0.05)	1.0128	1.0097	1.103×10^{-1}
	100×100 (0.02)	1.0060	1.0035	7.035×10^{-2}
	200×200 (0.01)	1.0036	1.0014	4.989×10^{-2}
20×20	10×10 (2.0)	1.0004	0.9992	7.786×10^{-2}
(Φ_α and H)	20×20 (1.0)	1.0006	0.9995	5.983×10^{-2}
	40×40 (0.5)	1.0006	0.9994	4.401×10^{-2}
	100×100 (0.2)	1.0007	0.9995	2.855×10^{-2}
	200×200 (0.1)	1.0008	0.9995	2.039×10^{-2}
20×20	10×10 (2.0)	1.0449	1.0432	2.247×10^{-1}
(H)	20×20 (1.0)	1.0233	1.0212	1.600×10^{-1}
	40×40 (0.5)	1.0124	1.0104	1.143×10^{-2}
	100×100 (0.2)	1.0058	1.0039	7.333×10^{-2}
	200×200 (0.1)	1.0035	1.0017	5.242×10^{-2}

- compute SIFs for a wide range of material mismatch combinations; and
- examine accuracy under both pure tension and pure shear loading conditions.

We first consider the case of pure tension remote loading. In the numerical model, we use symmetry and only half the specimen is considered (Figure 6) with appropriate displacement boundary conditions to remove rigid-body modes. The right-hand edge is fixed in the x-direction to remove the edge singularity [21]. The factors K_0 and $\mathcal{G}_0$ are used to normalize the stress intensity factors and the energy release rate, respectively,

$$K_0 = \sigma_{22}^\infty \sqrt{\pi a}, \quad \mathcal{G}_0 = \frac{(\sigma_{22}^\infty)^2 a}{E_2} \tag{24}$$

where $2a$ is the crack length. The material constants used in the numerical computations are: $E_1/E_2 = 22$, $v_1 = 0.2571$ and $v_2 = 0.3$ [24], and plane strain conditions are assumed. The exact solution from Equation (23) is

$$\frac{K_1}{K_0} = 1.008, \quad \frac{K_2}{K_0} = -0.1097, \quad \frac{\mathcal{G}}{\mathcal{G}_0} = 1.4358 \tag{25}$$

In Table II, the results of the domain independence study are listed. The domain radius $r_d = r_k h_e$, where r_k is a scalar multiple and h_e is the crack-tip element size. The sample size chosen
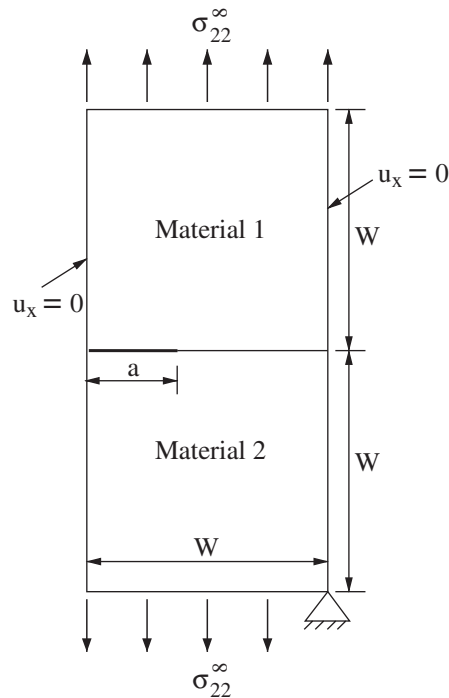
Figure 6. Centre-crack under remote tension (half-model).

Table II. Centre-crack under remote tension: domain independence study ($W/a = 20$).

h_e/a	r_k	K_1/K_0 (% Error)	K_2/K_0 (% Error)	$\mathscr{G}/\mathscr{G}_0$ (% Error)
0.1	2	1.011 (0.3)	−0.1145 (4.4)	1.445 (0.6)
[Q4]	3	1.010 (0.2)	−0.1121 (2.2)	1.441 (0.3)
	4	1.010 (0.2)	−0.1115 (1.6)	1.442 (0.4)
	5	1.010 (0.2)	−0.1113 (1.5)	1.442 (0.4)
	6	1.010 (0.2)	−0.1113 (1.5)	1.442 (0.4)
0.2	2	1.011 (0.4)	−0.1154 (5.2)	1.445 (0.6)
[Q4]	3	1.009 (0.1)	−0.1132 (3.2)	1.440 (0.3)
	4	1.010 (0.2)	−0.1126 (2.6)	1.442 (0.4)
0.2	2	1.008 (0.0)	−0.1211 (10.4)	1.439 (2.7)
[TRI3]	3	1.010 (0.2)	−0.1157 (5.5)	1.443 (0.5)
	4	1.009 (0.1)	−0.1116 (1.7)	1.438 (0.2)

is $W/a = 20$. Results are listed for two different values of h_e/a (rectangular, Q4): $h_e/a = 0.1$ corresponds to a 200×400 finite element mesh, whereas $h_e/a = 0.2$ is for a 100×200 mesh. In addition, an unstructured (triangular, TRI3) mesh is also considered to demonstrate the flexibility of the X-FEM. In Figure 7, the rectangular (20 000 elements) and triangular (46 088 elements) finite element meshes in the vicinity of the crack are shown ($a = 1$); the domain is 20×40. We observe domain independence of the SIFs for $r_k > 3$ and $r_k > 4$ on structured and
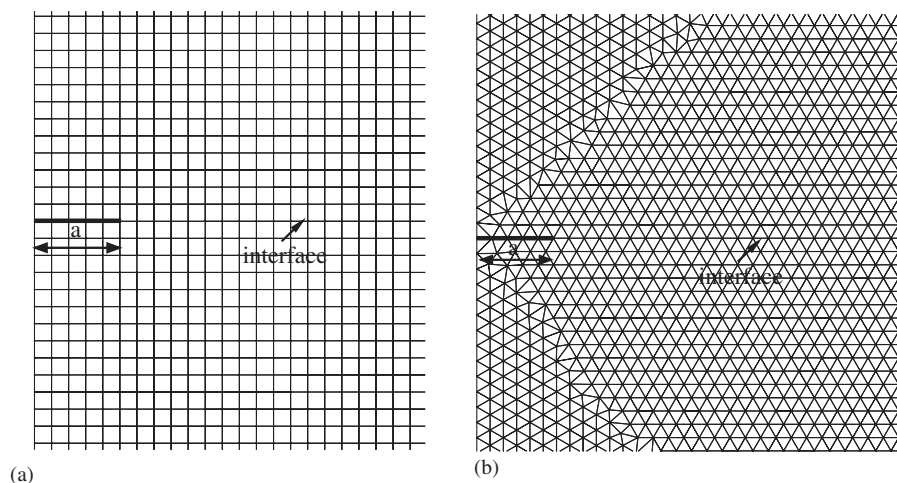
Figure 7. Structured and unstructured meshes in the vicinity of the crack ($a = 1$).

Table III. Centre-crack under remote tension: robustness study.

Crack-tip perturbation Δ/a	K_1/K_0 (% Error)	K_2/K_0 (% Error)	$\mathcal{G}/\mathcal{G}_0$ (% Error)
0	1.010 (0.2)	−0.1126 (2.6)	1.442 (0.4)
−0.001	1.009 (0.1)	−0.1113 (1.5)	1.443 (0.5)
0.001	1.009 (0.1)	−0.1130 (3.0)	1.445 (0.6)

unstructured meshes, respectively; the mixed-mode stress intensity factors are in good agreement with the exact solution. The K_1 values are markedly more accurate than K_2; the error in K_1 is a fraction of a per cent whereas the error in K_2 is about 1.5 per cent. It might appear that the accuracy of the SIFs hinges on the use of very refined meshes. We point out that the mesh size in the vicinity of the crack is $a/5$ or $a/10$, and for ease of mesh generation, we chose to use the same mesh spacing in the entire domain. The use of Cartesian meshes that are coarser away from the crack would lead to a dramatic decrease in the total number of elements without significantly impacting the accuracy of the stress intensity factor computations.

To study the robustness of the method, a simple test is conducted. The crack-tip location is perturbed by $\pm\Delta/a$ and the SIF results are compared to that when $\Delta = 0$. The specimen and mesh parameters are $W/a = 20$, $h_e/a = 0.2$ and $r_k = 4$. Numerical computations are carried out for $\Delta/a = \pm 0.001$. The results are shown in Table III, along with the case for $\Delta = 0$ which is reproduced from Table II. When $\Delta = 0$, the crack tip lies on a node, and nine nodes are enriched by the near-tip functions, whereas for $\Delta/a = \pm 0.001$, six nodes are enriched by the near-tip asymptotic fields. From Table III, we observe that for small perturbations, the SIFs and the energy release rate are accurate and stable.

Since the reference solution is for the infinite domain problem, we also probed the SIF trends when the ratio W/a was increased. The results are tabulated in Table IV. As expected, with

Table IV. Centre-crack under remote tension: finite specimen effects.

h_e/a	W/a	K_1/K_0 (% Error)	K_2/K_0 (% Error)	$\mathcal{G}/\mathcal{G}_0$ (% Error)
0.1	5	1.040 (3.17)	−0.1123 (2.37)	1.529 (6.49)
[$r_k = 8$]	10	1.017 (0.89)	−0.1116 (1.73)	1.460 (1.68)
	20	1.010 (0.20)	−0.1112 (1.37)	1.443 (0.50)
	30	1.009 (0.10)	−0.1110 (1.19)	1.440 (0.29)
0.2	5	1.040 (3.17)	−0.1138 (3.73)	1.529 (6.49)
[$r_k = 4$]	10	1.016 (0.79)	−0.1131 (3.10)	1.459 (1.61)
	20	1.010 (0.20)	−0.1126 (2.64)	1.442 (0.43)
	40	1.008 (0.00)	−0.1125 (2.55)	1.438 (0.15)
	60	1.008 (0.00)	−0.1122 (2.28)	1.437 (0.08)

Table V. Centre-crack under remote tension: material mismatch study.

E_1/E_2	α	β	X-FEM K_1/K_0 (% Error)	K_2/K_0 (% Error)	$\mathcal{G}/\mathcal{G}_0$ (% Error)	Exact solution K_1/K_0	K_2/K_0	$\mathcal{G}/\mathcal{G}_0$
2	0.333	0.095	1.002 (0.1)	−0.0411 (3.5)	2.136 (0.1)	1.001	−0.0397	2.133
4	0.600	0.171	1.004 (0.1)	−0.0743 (3.2)	1.758 (0.2)	1.003	−0.072	1.755
8	0.778	0.222	1.007 (0.2)	−0.0967 (3.0)	1.563 (0.3)	1.005	−0.0939	1.560
20	0.905	0.259	1.009 (0.1)	−0.1127 (2.6)	1.443 (0.2)	1.008	−0.1098	1.440
40	0.951	0.272	1.010 (0.1)	−0.1185 (2.4)	1.402 (0.2)	1.009	−0.1157	1.400
100	0.980	0.280	1.010 (0.0)	−0.1220 (2.2)	1.377 (0.1)	1.010	−0.1194	1.375
1000	0.998	0.285	1.010 (0.0)	−0.1239 (1.9)	1.361 (0.1)	1.010	−0.1216	1.360

increase in W/a, the numerically computed results for K_1 and K_2 tend to the exact solution. For $W/a > 20$, finite specimen effects are negligible, and hence specimen dimensions of that order or larger can be used with confidence to model the infinite domain problem. In Table II, accurate SIFs were obtained for a particular bimaterial. Now, we study the performance of the X-FEM for different bimaterial combinations. The specimen size $W/a = 30$ and a finite element mesh with $h_e/a = 0.2$ is used. The scalar multiple r_k is set to 4 in the domain integral computations. The results of the material mismatch study are presented in Table V, where the ratio E_1/E_2 was varied from 2 to 1000. It can be observed that the results are accurate to within a few per cent, with the accuracy maintained even when material 1 is much stiffer than material 2 (large mismatch).

Next, we consider the bimaterial plate problem under remote shear tractions. The specimen dimensions, crack configuration, and the external shear tractions for the full model are indicated in Figure 8. Under pure shear, theory predicts that interpenetration (contact) of crack faces occurs, but as argued by Rice [21], the K-field solution can still be used since the contact zone is extremely small (sub-atomic) for bimaterial combinations and loading configurations that are of practical interest. For the case of shear loading, all studies are conducted using a sample size $W/a = 30$ and $h_e/a = 0.2$ (300×300 mesh). In addition, it is assumed that the parameter $r_k = 4$, unless stated to be otherwise. Here too, we begin with a domain independence study and use the same material parameters as before: $E_1/E_2 = 22$, $v_1 = 0.2571$ and $v_2 = 0.3$ [24].
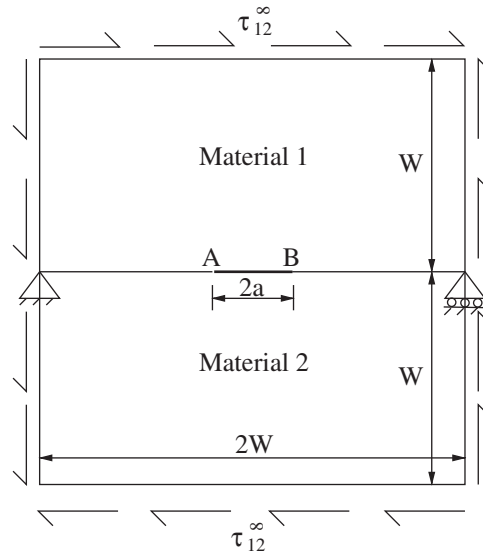
Figure 8. Centre-crack under remote shear.

Table VI. Centre-crack under remote shear: domain independence study.

Crack-tip	r_k	K_1/K_0 (% Error)	K_2/K_0 (% Error)	$\mathscr{G}/\mathscr{G}_0$ (% Error)
Left (*A*)	2	-3.505×10^{-2} (10.6)	1.016 (0.2)	1.444 (0.6)
	3	-3.267×10^{-2} (3.1)	1.015 (0.1)	1.440 (0.3)
	4	-3.096×10^{-2} (2.3)	1.016 (0.2)	1.442 (0.4)
Right (*A*)	2	3.224×10^{-2} (1.7)	1.014 (0.04)	1.437 (0.1)
	3	3.129×10^{-2} (1.3)	1.015 (0.1)	1.441 (0.3)
	4	3.025×10^{-2} (4.6)	1.016 (0.2)	1.442 (0.4)

The exact solution under pure shear external loading ($\sigma_{22}^\infty = 0$) is obtained from Equation (23):

$$K_0 = \tau_{12}^\infty \sqrt{\pi a}, \quad \mathscr{G}_0 = \frac{(\tau_{12}^\infty)^2 a}{E_2} \tag{26}$$

$$\frac{K_1}{K_0} = \pm 0.0317, \quad \frac{K_2}{K_0} = 1.0136, \quad \frac{\mathscr{G}}{\mathscr{G}_0} = 1.436 \tag{27}$$

where K_1 is positive at the right crack tip *B* and negative at the left crack tip *A*. In Table VI, domain independence in the SIFs is studied. We observe domain independence of the SIFs for $r_k > 3$ and the normalized K_1 and K_2 are in good agreement with the exact solution. It is striking that K_2 is also accurate, even though it is more than an order of magnitude smaller than K_1. Results of the material mismatch study are presented in Table VII. For $E_1/E_2 = 2$–1000, it is observed that the normalized K_1 and K_2 computed by the X-FEM are in good agreement with the exact solution (maximum error in K_2 is a fraction of a per cent). We also note that K_1 is accurate, even though it is more than an order of magnitude smaller than K_2.

Table VII. Centre-crack under remote shear: material mismatch study.

E_1/E_2	α	β	X-FEM			Exact solution		
			K_1/K_0 (% Error)	K_2/K_0 (% Error)	$\mathcal{G}/\mathcal{G}_0$ (% Error)	K_1/K_0	K_2/K_0	$\mathcal{G}/\mathcal{G}_0$
2	0.333	0.095	0.0107 (9.3)	1.006 (0.4)	2.151 (0.8)	0.0118	1.002	2.133
4	0.600	0.171	0.0194 (8.5)	1.009 (0.3)	1.768 (0.7)	0.0212	1.006	1.755
8	0.778	0.222	0.0255 (6.9)	1.013 (0.3)	1.569 (0.6)	0.0274	1.010	1.560
20	0.905	0.259	0.0302 (5.0)	1.016 (0.2)	1.446 (0.4)	0.0318	1.014	1.440
40	0.951	0.272	0.0321 (3.6)	1.017 (0.2)	1.404 (0.3)	0.0333	1.015	1.400
100	0.980	0.280	0.0335 (2.3)	1.017 (0.1)	1.378 (0.2)	0.0343	1.016	1.375
1000	0.998	0.285	0.0347 (0.6)	1.018 (0.1)	1.363 (0.2)	0.0349	1.017	1.360
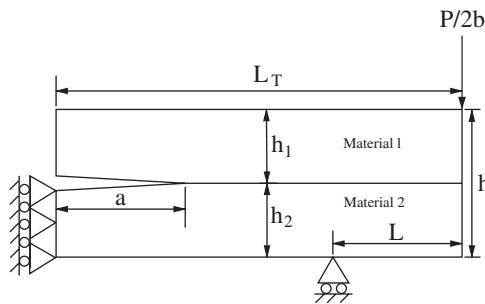
Figure 9. Bimaterial four-point bending specimen (half-model).

7.3. Bimaterial four-point bending specimen

In Reference [50], a bimaterial four-point bending test specimen was devised to measure interfacial fracture resistance. Theoretical solutions for the steady-state energy release rate were derived, and in addition finite element computations were also carried out [50]. The extraction of K_1 and K_2 for the four-point bending specimen, and the computation of the phase angle ψ was also conducted in Reference [24]. We compare the X-FEM solution to the results obtained in the above studies. Owing to symmetry in the loading and in the crack configuration (symmetrical interfacial cracks), we use one-half of the specimen in the numerical model. The specimen dimensions, crack orientation, loading and the displacement boundary conditions are indicated in Figure 9. The thickness of the upper layer is h_1 and that of the lower layer is h_2, with the total thickness denoted by h. We use E_1 and v_1 to denote Young's modulus and Poisson's ratio of the upper layer, respectively, and E_2 and v_2 are the corresponding properties for the layer below the crack.

When the interface crack length significantly exceeds the thickness of the upper layer, steady-state conditions are reached and the energy release rate stabilizes to a constant value, $\mathcal{G}_{ss}$, the steady-state energy release rate. Charalambides *et al.* [50] used beam theory analysis to arrive at the following expression for

$$\mathcal{G}_{ss} = \frac{3(1-v_2^2)P^2L^2}{2E_2b^2h^3}\left\{\left(\frac{h}{h_2}\right)^3 - \lambda\left[\left(\frac{h_1}{h}\right)^3 + \lambda\left(\frac{h_2}{h}\right)^3 + 3\lambda\frac{h_1h_2}{h^2}\left(\frac{h_1}{h}+\lambda\frac{h_2}{h}\right)^{-1}\right]^{-1}\right\} \quad (28a)$$

Table VIII. Bimaterial four-point bending problem: effect of element size for
elastic moduli ratio $E_1/E_2 = 10$ and $v_1 = v_2 = 0.3$.

h_e/h_1	Analytical	X-FEM			
	$\mathcal{G}/\mathcal{G}_0$	$\mathcal{G}/\mathcal{G}_0$ (% Error)	K_1/K_0	K_2/K_0	ψ
0.1	1.363	1.371 (0.56)	0.902	1.350	43.258
0.125	1.363	1.373 (0.69)	0.902	1.351	43.258
0.2	1.363	1.379 (1.14)	0.904	1.354	43.258

where

$$\lambda = \frac{E_2(1 - v_1^2)}{E_1(1 - v_2^2)} \tag{28b}$$

We choose the factors K_0 and $\mathcal{G}_0$ to normalize the SIFs and the energy release rate, respectively,

$$K_0 = \frac{PL}{bh^{3/2}}, \quad \mathcal{G}_0 = \frac{(1 - v_2^2)P^2L^2}{E_2 b^2 h^3} \tag{29}$$

In the numerical model, we take the width b to be unity, $L_T/L = 2.5$, $L/h = 5$, and plane strain conditions are assumed. In addition, the phase angle is determined by taking the characteristic length ℓ given in Equation (4) to be the total beam thickness h:

$$\psi = \tan^{-1}\left(\frac{\texttt{Im}[\mathbf{K}h^{i\varepsilon}]}{\texttt{Re}[\mathbf{K}h^{i\varepsilon}]}\right) \tag{30}$$

First, we study the effect of element size on $\mathcal{G}_{ss}$. A fixed thickness ratio $h_1/h = \frac{1}{10}$ is used, and the ratio h_e/h_1 (regular structured mesh) is varied. The material parameters are $E_1/E_2 = 10$, $v_1 = v_2 = 0.3$. In addition, $a/h = 3$ and we set $r_k = 4$. The problem domain is $L_T \times h \equiv 125 \times 10$, $h_1 = 1$ and $a = 30$. Comparisons between the X-FEM results and the reference solution [50] for $\mathcal{G}_{ss}/\mathcal{G}_0$ are presented in Table VIII; the X-FEM results for K_1, K_2 and ψ are also indicated for completeness. From the results given in Table VIII, we observe that the X-FEM results are in good agreement with the reference solution, and the correspondence improves with mesh refinement. In Table IX, the steady-state energy release rate is listed for different thickness ratios h_1/h, which range from 0.1 to 0.5. The Poisson ratios of the layers are taken to be the same: $v_1 = v_2 = 0.3$. Once again, the X-FEM result is in excellent agreement with the reference solution; errors in the normalized $\mathcal{G}_{ss}$ are less than 1 per cent. When the lower layer is stiffer ($E_1/E_2 = 1/10$), the phase angle $\psi = 46.6°$ for the case $h_1/h = 0.5$ matches the result $\psi = 46.3°$ obtained by Matos *et al.* [24].

8. CONCLUSIONS

In this paper, we have proposed a partition of unity enrichment technique for bimaterial interface cracks. This work has extended the capabilities of the extended finite element method to the analysis of cracks that lie at the interface of two elastically homogeneous isotropic materials. A discontinuous function and the 2D near-tip asymptotic displacement functions were added

Table IX. Bimaterial four-point bending problem: effect of thickness ratio for $v_1 = v_2 = 0.3$.

E_1/E_2	h_1/h	Analytical $\mathcal{G}/\mathcal{G}_0$	X-FEM $\mathcal{G}/\mathcal{G}_0$ (% Error)	K_1/K_0	K_2/K_0	ψ
10	0.1	1.363	1.372 (0.69)	0.903	1.351	43.258
	0.2	2.279	2.292 (0.57)	1.220	1.708	41.448
	0.3	3.725	3.747 (0.59)	1.686	2.089	38.102
	0.4	6.325	6.365 (0.63)	2.358	2.585	34.612
	0.5	11.450	11.540 (0.73)	3.346	3.315	31.742
	0.1	0.0807	0.0811 (0.43)	0.078	0.097	64.15
	0.2	0.3043	0.3051 (0.26)	0.172	0.171	57.88
0.1	0.3	0.9010	0.9026 (0.19)	0.318	0.269	49.53
	0.4	2.4655	2.4703 (0.20)	0.554	0.410	49.53
	0.5	6.5223	6.5297 (0.11)	0.934	0.620	46.60

to the finite element approximation using the framework of partition of unity. The crack-tip enrichment functions were chosen as those that span the asymptotic displacement fields for an interfacial crack. The concept of partition of unity facilitated the incorporation of the oscillatory nature of the singularity within a conforming finite element approximation. The stress intensity factors for bimaterial interfacial cracks were numerically evaluated using the domain form of the interaction integral. In all numerical examples, structured meshes were adopted and a relatively coarse mesh discretization was used in the vicinity of the crack tip (5–10 elements spanned the crack). A convergence study was first conducted by imposing the near-tip displacement field on the boundary of a bimaterial specimen. The crack was located along the interface, starting from the edge and terminating at the centre of the specimen. With refinement, the K-field solution ($K_1 = 1$, $K_2 = 1$) was recovered, which provided a suitable test for the implementation of the method. From the relative error in the energy norm, the rate of convergence of the method was estimated to be *one-half*, which matches the theoretical convergence rate of the classical FEM in the presence of a dominant $\sqrt{r}$-singularity [43]. As a benchmark problem, the bimaterial plate with a centre crack was considered and numerical results for the SIFs were compared to the theoretical solution [20, 21]; excellent agreement was obtained for a wide range of material combinations and for both pure tension and pure shear far-field loading. The steady-state energy release rate for the bimaterial, notched four-point bending specimen was found to be in good agreement with the reference solution [50]; stable versus unstable crack propagation in the four-point bending specimen is currently under investigation. The modelling capabilities and notable accuracy realized through the proposed technique point to its potential to study complex interfacial failure processes in multi-layered dissimilar isotropic as well as anisotropic [51] material systems.

APPENDIX A

The Cartesian derivatives of the near-tip enrichment functions $[\Phi_\alpha(\mathbf{x}), \alpha = 1\text{--}12]$ are given below.

$$\frac{\partial \Phi_1}{\partial x} = -\frac{e^{-\varepsilon\theta} \sin \theta/2}{2\sqrt{r}} \{\cos(\varepsilon \log r) + 2\varepsilon \sin(\varepsilon \log r - \theta)\} \qquad \text{(A1a)}$$

$$\frac{\partial \Phi_1}{\partial y} = \frac{e^{-\varepsilon\theta}}{2\sqrt{r}}\{\cos(\varepsilon \log r) \cos \theta/2 - 2\varepsilon \cos(\varepsilon \log r - \theta) \sin \theta/2\} \tag{A1b}$$

$$\frac{\partial \Phi_2}{\partial x} = \frac{e^{-\varepsilon\theta} \cos \theta/2}{2\sqrt{r}}\{\cos(\varepsilon \log r) - 2\varepsilon \sin(\varepsilon \log r - \theta)\} \tag{A2a}$$

$$\frac{\partial \Phi_2}{\partial y} = \frac{e^{-\varepsilon\theta}}{2\sqrt{r}}\{\cos(\varepsilon \log r) \sin \theta/2 - 2\varepsilon \cos(\varepsilon \log r - \theta) \cos \theta/2\} \tag{A2b}$$

$$\frac{\partial \Phi_3}{\partial x} = -\frac{e^{\varepsilon\theta} \sin \theta/2}{2\sqrt{r}}\{\cos(\varepsilon \log r) + 2\varepsilon \sin(\varepsilon \log r + \theta)\} \tag{A3a}$$

$$\frac{\partial \Phi_3}{\partial y} = \frac{e^{\varepsilon\theta}}{2\sqrt{r}}\{\cos(\varepsilon \log r) \cos \theta/2 + 2\varepsilon \cos(\varepsilon \log r + \theta) \sin \theta/2\} \tag{A3b}$$

$$\frac{\partial \Phi_4}{\partial x} = \frac{e^{\varepsilon\theta} \cos \theta/2}{2\sqrt{r}}\{\cos(\varepsilon \log r) - 2\varepsilon \sin(\varepsilon \log r + \theta)\} \tag{A4a}$$

$$\frac{\partial \Phi_4}{\partial y} = \frac{e^{\varepsilon\theta}}{2\sqrt{r}}\{\cos(\varepsilon \log r) \sin \theta/2 + 2\varepsilon \cos(\varepsilon \log r + \theta) \cos \theta/2\} \tag{A4b}$$

$$\frac{\partial \Phi_5}{\partial x} = -\frac{e^{\varepsilon\theta} \sin \theta}{2\sqrt{r}}\{\cos(\varepsilon \log r) \sin 3\theta/2 + 2\varepsilon \sin(\varepsilon \log r + \theta) \sin \theta/2\} \tag{A5a}$$

$$\frac{\partial \Phi_5}{\partial y} = \frac{e^{\varepsilon\theta}}{2\sqrt{r}}\{\cos(\varepsilon \log r)[\sin \theta/2 + \sin 3\theta/2 \cos \theta]$$

$$+ 2\varepsilon \cos(\varepsilon \log r + \theta) \sin \theta/2 \sin \theta\} \tag{A5b}$$

$$\frac{\partial \Phi_6}{\partial x} = -\frac{e^{\varepsilon\theta} \sin \theta}{2\sqrt{r}}\{\cos(\varepsilon \log r) \cos 3\theta/2 + 2\varepsilon \sin(\varepsilon \log r + \theta) \cos \theta/2\} \tag{A6a}$$

$$\frac{\partial \Phi_6}{\partial y} = \frac{e^{\varepsilon\theta}}{2\sqrt{r}}\{\cos(\varepsilon \log r)[\cos \theta/2 + \cos 3\theta/2 \cos \theta]$$

$$+ 2\varepsilon \cos(\varepsilon \log r + \theta) \cos \theta/2 \sin \theta\} \tag{A6b}$$

$$\frac{\partial \Phi_7}{\partial x} = \frac{\mathrm{e}^{-\varepsilon\theta} \sin \theta/2}{2\sqrt{r}} \{-\sin(\varepsilon \log r) + 2\varepsilon \cos(\varepsilon \log r - \theta)\} \tag{A7a}$$

$$\frac{\partial \Phi_7}{\partial y} = \frac{\mathrm{e}^{-\varepsilon\theta}}{2\sqrt{r}} \{\sin(\varepsilon \log r) \cos \theta/2 - 2\varepsilon \sin(\varepsilon \log r - \theta) \sin \theta/2\} \tag{A7b}$$

$$\frac{\partial \Phi_8}{\partial x} = \frac{\mathrm{e}^{-\varepsilon\theta} \cos \theta/2}{2\sqrt{r}} \{\sin(\varepsilon \log r) + 2\varepsilon \cos(\varepsilon \log r - \theta)\} \tag{A8a}$$

$$\frac{\partial \Phi_8}{\partial y} = \frac{\mathrm{e}^{-\varepsilon\theta}}{2\sqrt{r}} \{\sin(\varepsilon \log r) \sin \theta/2 - 2\varepsilon \sin(\varepsilon \log r - \theta) \cos \theta/2\} \tag{A8b}$$

$$\frac{\partial \Phi_9}{\partial x} = \frac{\mathrm{e}^{\varepsilon\theta} \sin \theta/2}{2\sqrt{r}} \{-\sin(\varepsilon \log r) + 2\varepsilon \cos(\varepsilon \log r + \theta)\} \tag{A9a}$$

$$\frac{\partial \Phi_9}{\partial y} = \frac{\mathrm{e}^{\varepsilon\theta}}{2\sqrt{r}} \{\sin(\varepsilon \log r) \cos \theta/2 + 2\varepsilon \sin(\varepsilon \log r + \theta) \sin \theta/2\} \tag{A9b}$$

$$\frac{\partial \Phi_{10}}{\partial x} = \frac{\mathrm{e}^{\varepsilon\theta} \cos \theta/2}{2\sqrt{r}} \{\sin(\varepsilon \log r) + 2\varepsilon \cos(\varepsilon \log r + \theta)\} \tag{A10a}$$

$$\frac{\partial \Phi_{10}}{\partial y} = \frac{\mathrm{e}^{\varepsilon\theta}}{2\sqrt{r}} \{\sin(\varepsilon \log r) \sin \theta/2 + 2\varepsilon \sin(\varepsilon \log r + \theta) \cos \theta/2\} \tag{A10b}$$

$$\frac{\partial \Phi_{11}}{\partial x} = \frac{\mathrm{e}^{\varepsilon\theta} \sin \theta}{2\sqrt{r}} \{-\sin(\varepsilon \log r) \sin 3\theta/2 + 2\varepsilon \cos(\varepsilon \log r + \theta) \sin \theta/2\} \tag{A11a}$$

$$\frac{\partial \Phi_{11}}{\partial y} = \frac{\mathrm{e}^{\varepsilon\theta}}{2\sqrt{r}} \{\sin(\varepsilon \log r) \left[\sin \theta/2 + \sin 3\theta/2 \cos \theta\right]$$
$$+ 2\varepsilon \sin(\varepsilon \log r + \theta) \sin \theta/2 \sin \theta\} \tag{A11b}$$

$$\frac{\partial \Phi_{12}}{\partial x} = \frac{\mathrm{e}^{\varepsilon\theta} \sin \theta}{2\sqrt{r}} \{-\sin(\varepsilon \log r) \cos 3\theta/2 + 2\varepsilon \cos(\varepsilon \log r + \theta) \cos \theta/2\} \tag{A12a}$$

$$\frac{\partial \Phi_{12}}{\partial y} = \frac{\mathrm{e}^{\varepsilon\theta}}{2\sqrt{r}} \{\sin(\varepsilon \log r) \left[\cos \theta/2 + \cos 3\theta/2 \cos \theta\right]$$
$$+ 2\varepsilon \sin(\varepsilon \log r + \theta) \cos \theta/2 \sin \theta\} \tag{A12b}$$

APPENDIX B

In this appendix, we list the auxiliary fields [24] used in the domain integral computations. To extract the mixed-mode stress intensity factors K_1 and K_2, the auxiliary displacement field in the local x_1–x_2 crack-tip co-ordinate system (Figure 1) can be written as

$$u_i = \begin{cases} \dfrac{1}{4\mu_1 \cosh(\pi\varepsilon)} \sqrt{\dfrac{r}{2\pi}} f_i(r, \theta, \varepsilon, \kappa_1) & \text{(upper-half plane)} \\[4mm] \dfrac{1}{4\mu_2 \cosh(\pi\varepsilon)} \sqrt{\dfrac{r}{2\pi}} f_i(r, \theta, \varepsilon, \kappa_2) & \text{(lower-half plane)} \end{cases} \qquad (i = 1, 2) \qquad \text{(B1)}$$

where ε is the bimaterial constant that is defined in Equation (6b).

To extract K_1, the functions f_1 and f_2 are

$$f_1 = D + 2\delta \sin\theta \sin\varphi \equiv D + T_1, \quad f_2 = -C - 2\delta \sin\theta \cos\varphi \equiv -C - T_2 \qquad \text{(B2)}$$

whereas to compute K_2, the expressions for f_1 and f_2 are

$$f_1 = -C + 2\delta \sin\theta \cos\varphi \equiv -C + T_2, \quad f_2 = -D + 2\delta \sin\theta \sin\varphi \equiv -D + T_1 \qquad \text{(B3)}$$

In the above equations, δ, φ, C and D are defined as

$$\delta = \begin{cases} \mathrm{e}^{-(\pi-\theta)\varepsilon} & \text{(upper-half plane)} \\[2mm] \mathrm{e}^{(\pi+\theta)\varepsilon} & \text{(lower-half plane)} \end{cases} \qquad \varphi = \varepsilon \log r + \frac{\theta}{2} \qquad \text{(B4a)}$$

$$C = \beta'\gamma \cos\frac{\theta}{2} - \beta\gamma' \sin\frac{\theta}{2}, \quad D = \beta\gamma \cos\frac{\theta}{2} + \beta'\gamma' \sin\frac{\theta}{2} \qquad \text{(B4b)}$$

$$\beta = \frac{0.5 \cos(\varepsilon \log r) + \varepsilon \sin(\varepsilon \log r)}{0.25 + \varepsilon^2}, \quad \beta' = \frac{0.5 \sin(\varepsilon \log r) - \varepsilon \cos(\varepsilon \log r)}{0.25 + \varepsilon^2} \qquad \text{(B4c)}$$

$$\gamma = \kappa\delta - \frac{1}{\delta}, \quad \gamma' = \kappa\delta + \frac{1}{\delta}, \quad \kappa = \begin{cases} \kappa_1 & \text{(upper-half plane)} \\[2mm] \kappa_2 & \text{(lower-half plane)} \end{cases} \qquad \text{(B4d)}$$

where κ_1, κ_2 are defined in Equation (6c), and (r, θ) are polar co-ordinates as shown in Figure 1.

The auxiliary strain components are the symmetric gradient of the auxiliary displacement components:

$$\varepsilon_{ij}^{\text{aux}} = \tfrac{1}{2}(u_{i,j}^{\text{aux}} + u_{j,i}^{\text{aux}}), \quad (i, j = 1, 2) \qquad \text{(B5)}$$

We now proceed to present the displacement gradients of the auxiliary fields. To this end, we first obtain the derivatives of the expressions in Equations (B2) and (B3). Define

$$T_3 = 2\delta \cos\theta \sin\varphi, \quad T_4 = 2\delta \cos\theta \cos\varphi \qquad \text{(B6a)}$$

whence

$$T_{1,r} = \frac{\varepsilon T_2}{r}, \quad T_{1,\theta} = \varepsilon T_1 + \frac{T_2}{2} + T_3 \tag{B6b}$$

$$T_{2,r} = -\frac{\varepsilon T_1}{r}, \quad T_{2,\theta} = \varepsilon T_2 - \frac{T_1}{2} + T_4 \tag{B6c}$$

where T_1 and T_2 are given in Equations (B2) and (B3). On defining

$$E = \beta'\gamma' \cos\frac{\theta}{2} - \beta\gamma \sin\frac{\theta}{2}, \quad F = \beta\gamma' \cos\frac{\theta}{2} + \beta'\gamma \sin\frac{\theta}{2} \tag{B7a}$$

we have

$$C_{,r} = \frac{\varepsilon D}{r}, \quad C_{,\theta} = -\frac{F}{2} + \varepsilon E \tag{B7b}$$

$$D_{,r} = -\frac{\varepsilon C}{r}, \quad D_{,\theta} = \frac{E}{2} + \varepsilon F \tag{B7c}$$

If K_1 is to be extracted, then

$$f_{1,\alpha} = D_{,\alpha} + T_{1,\alpha}, \quad f_{2,\alpha} = -C_{,\alpha} - T_{2,\alpha} \quad (\alpha = r, \theta) \tag{B8}$$

whereas if K_2 is to be computed, then

$$f_{1,\alpha} = -C_{,\alpha} + T_{2,\alpha}, \quad f_{2,\alpha} = -D_{,\alpha} + T_{1,\alpha} \quad (\alpha = r, \theta) \tag{B9}$$

Since $r_{,1} = \cos\theta$, $r_{,2} = \sin\theta$, $\theta_{,1} = -\sin\theta/r$ and $\theta_{,2} = \cos\theta/r$, on using the chain rule, we can write the derivatives of f_1 and f_2 in the x_1–x_2 co-ordinate system as

$$f_{1,1} = f_{1,r}r_{,1} + f_{1,\theta}\theta_{,1}, \quad f_{1,2} = f_{1,r}r_{,2} + f_{1,\theta}\theta_{,2} \tag{B10a}$$

$$f_{2,1} = f_{2,r}r_{,1} + f_{2,\theta}\theta_{,1}, \quad f_{2,2} = f_{2,r}r_{,2} + f_{2,\theta}\theta_{,2} \tag{B10b}$$

Letting

$$A = \begin{cases} \dfrac{1}{4\mu_1 \cosh(\pi\varepsilon)} & \text{(upper half-plane)} \\[2mm] \dfrac{1}{4\mu_2 \cosh(\pi\varepsilon)} & \text{(lower half-plane)} \end{cases} \qquad B = \sqrt{\frac{r}{2\pi}} \tag{B11}$$

we can now write the gradients of the auxiliary displacements as

$$u_{1,1}^{\text{aux}} = A\left(Bf_{1,1} + \frac{r_{,1}f_1}{4\pi B}\right) \tag{B12a}$$

$$u_{1,2}^{\text{aux}} = A\left(Bf_{1,2} + \frac{r_{,2}f_1}{4\pi B}\right) \tag{B12b}$$

$$u_{2,1}^{\mathrm{aux}} = A\left(Bf_{2,1} + \frac{r_{,1}f_2}{4\pi B}\right) \tag{B12c}$$

$$u_{2,2}^{\mathrm{aux}} = A\left(Bf_{2,2} + \frac{r_{,2}f_2}{4\pi B}\right) \tag{B12d}$$

and the auxiliary strains can now be evaluated from Equation (B5). Using Hooke's law, the auxiliary stresses $\sigma_{ij}^{\mathrm{aux}}$ are computed from the auxiliary strains.

REFERENCES

1. Evans AG. Perspectives on the development of high-toughness ceramics. *Journal of the American Ceramic Society* 1990; **73**:187–206.
2. Hutchinson JW, Suo Z. Mixed mode cracking in layered materials. In *Advances in Applied Mechanics*, Hutchinson JW, Wu TY (eds), vol. 29. Academic Press: Orlando, 1992; 63–191.
3. Henshell RD, Shaw KG. Crack tip finite elements are unnecessary. *International Journal for Numerical Methods in Engineering* 1975; **9**:495–507.
4. Barsoum RS. On the use of isoparametric finite elements in linear fracture mechanics. *International Journal for Numerical Methods in Engineering* 1976; **10**:551–564.
5. Barsoum RS. Triangular quarter-point elements as elastic and perfectly-plastic crack tip elements. *International Journal for Numerical Methods in Engineering* 1977; **11**:85–98.
6. Zak AR, Williams ML. Crack point singularities at a bimaterial interface. *Journal of Applied Mechanics* 1963; **30**: 142–143.
7. Cook TS, Erdogan F. Stresses in bonded materials with a crack perpendicular to the crack. *International Journal of Engineering Science* 1972; **10**:677–697.
8. Dundurs J. Edge-bonded dissimilar orthogonal elastic wedges. *Journal of Applied Mechanics* 1969; **36**: 650–652.
9. Akin JE. The generation of elements with singularities. *International Journal for Numerical Methods in Engineering* 1976; **10**:1249–1259.
10. Benzley SE. Representation of singularities with isoparametric finite elements. *International Journal for Numerical Methods in Engineering* 1974; **8**:537–545.
11. Tracey DM, Cook TS. Analysis of power type singularities using finite elements. *International Journal for Numerical Methods in Engineering* 1977; **11**:1225–1233.
12. Gifford Jr. LN, Hilton PD. Stress intensity factors by enriched finite elements. *Engineering Fracture Mechanics* 1978; **10**:485–496.
13. Stern M. Families of consistent elements with singular derivative fields. *International Journal for Numerical Methods in Engineering* 1979; **14**:409–422.
14. Hughes TJR, Stern M. Techniques for developing special finite element shape functions with particular references to singularities. *International Journal for Numerical Methods in Engineering* 1980; **15**:733–751.
15. Abdi RE, Valentin G. Isoparametric elements for crack normal to the bi-material interface. *Computers and Structures* 1989; **33**:241–248.
16. Lim W.-K, Lee C.-S. Evaluation of stress intensity factors for a crack normal to a bimaterial interface using isoparamteric finite elements. *Engineering Fracture Mechanics* 1995; **62**:65–70.
17. Yavari A, Sarkani S, Moyer Jr. ET. On quadratic isoparametric transition elements for a crack normal to a bimaterial interface. *International Journal for Numerical Methods in Engineering* 1999; **46**:457–469.

18. Atluri SN, Nakagaki M. Computational methods for plane problems of fracture. In *Computational Methods in the Mechanics of Fracture*, Atluri SN (ed.), vol. 2. North-Holland: Amsterdam, The Netherlands, 1986; 169–227.
19. Williams ML. The stress around a fault or crack in dissimilar media. *Bulletin of the Seismology Society of America* 1959; **49**:199–204.
20. Rice JR, Sih GC. Plane problems of cracks in dissimilar media. *Journal of Applied Mechanics* 1965; **32**: 418–423.
21. Rice JR. Elastic fracture mechanics concepts for interfacial cracks. *Journal of Applied Mechanics* 1988; **55**: 98–103.
22. Yau JF, Wang SS. An analysis of interface cracks between dissimilar isotropic material using conservation integrals in elasticity. *Engineering Fracture Mechanics* 1984; **20**:423–432.
23. Shih CF, Asaro RJ. Elastic-plastic analysis of cracks on bimaterial interfaces: Part I—small scale yielding. *Journal of Applied Mechanics* 1988; **55**:299–316.
24. Matos PPL, McMeeking RM, Charalambides PG, Drory MD. A method for calculating stress intensities in bimaterial fracture. *International Journal of Fracture* 1989; **40**:235–254.
25. Nahta R, Moran B. Domain integrals for axisymmetric interface crack problems. *International Journal of Solids and Structures* 1993; **30**(15):2027–2040.
26. Bjerkén C, Persson C. A numerical method for calculating stress intensity factors for interface cracks in bimaterials. *Engineering Fracture Mechanics* 2001; **68**:235–246.
27. Yau JF, Wang SS, Corten HT. A mixed-mode crack analysis of isotropic solids using conservation laws of elasticity. *Journal of Applied Mechanics* 1980; **47**:335–341.
28. Belytschko T, Black T. Elastic crack growth in finite elements with minimal remeshing. *International Journal for Numerical Methods in Engineering* 1999; **45**(5):601–620.
29. Moës N, Dolbow J, Belytschko T. A finite element method for crack growth without remeshing. *International Journal for Numerical Methods in Engineering* 1999; **46**(1):131–150.
30. Daux C, Moës N, Dolbow J, Sukumar N, Belytschko T. Arbitrary cracks and holes with the extended finite element method. *International Journal for Numerical Methods in Engineering* 2000; **48**(12):1741–1760.
31. Belytschko T, Moës N, Usui S, Parimi C. Arbitrary discontinuities in finite elements. *International Journal for Numerical Methods in Engineering* 2001; **50**(4):993–1013.
32. Sukumar N, Prévost J.-H. Modeling quasi-static crack growth with the extended finite element method. Part I: Computer implementation. *International Journal of Solids and Structures* 2003; **40**(26):7513–7537.
33. Huang R, Sukumar N, Prévost J.-H. Modeling quasi-static crack growth with the extended finite element method. Part II: Numerical applications. *International Journal of Solids and Structures* 2003; **40**(26): 7539–7552.
34. Prévost J.-H. *Dynaflow*. Princeton University, Princeton, NJ 08544, 1983 (Updated Version: 2002).
35. Rice JR, Suo Z, Wang JS. Mechanics and thermodynamics of brittle interfacial failure in bimaterial systems. In *Metal–Ceramic Interfaces*, Ruhle M, Evans AG, Ashby MF, Hirth JP (eds). Pergamon Press: New York, NY, 1990; 269–294.
36. Shih CF. Cracks on bimaterial interfaces: elasticity and plasticity aspects. *Materials Science and Engineering* 1991; **A143**:77–90.
37. Malyshev BM, Salganik RL. The strength of adhesive joints using the theory of cracks. *International Journal of Fracture* 1965; **1**:114–128.
38. Suo Z. Mechanics of interface fracture. *Ph.D. Thesis*, Division of Applied Sciences, Harvard University, Cambridge, MA, U.S.A., 1989.
39. Melenk JM, Babuška I. The partition of unity finite element method: basic theory and applications. *Computer Methods in Applied Mechanics and Engineering* 1996; **139**:289–314.
40. Strouboulis T, Copps K, Babuška I. The generalized finite element method. *Computer Methods in Applied Mechanics and Engineering* 2001; **190**(32–33):4081–4193.
41. Duarte CA, Hamzeh ON, Liszka TJ, Tworzydlo WW. The element partition method for the simulation of three-dimensional dynamic crack propagation. *Computer Methods in Applied Mechanics and Engineering* 2001; **119**(15–17):2227–2262.
42. Fix G, Gulati S, Wakoff GI. On the use of singular functions with the finite element method. *Journal of Computational Physics* 1973; **13**:209–228.
43. Strang G, Fix G. *An Analysis of the Finite Element Method*. Prentice-Hall: Englewood Cliffs, NJ, 1973.
44. Huang R, Prévost JH, Huang ZY, Suo Z. Channel-cracking of thin films with the extended finite element method. *Engineering Fracture Mechanics* 2002; **70**(18):2513–2526.

45. Moran B, Shih CF. Crack tip and associated domain integrals from momentum and energy balance. *Engineering Fracture Mechanics* 1987; **27**(6):615–641.
46. Eshelby JD. Energy relations and the energy momentum tensor in continuum mechanics. In *Inelastic Behavior of Solids*, Kanninen MF, Adler WF, Rosenfeld AR, Jafee RT (eds). McGraw-Hill, Inc.: New York, 1970; 77–114.
47. Smelser RE. On the J-Integral for bi-material bodies. *International Journal of Fracture* 1977; **13**:382–384.
48. Li FZ, Shih CF, Needleman A. A comparison of methods for calculating energy release rates. *Engineering Fracture Mechanics* 1985; **21**(2):405–421.
49. Sukumar N, Chopp DL, Moës N, Belytschko T. Modeling holes and inclusions by level sets in the extended finite-element method. *Computer Methods in Applied Mechanics and Engineering* 2001; **190**(46–47): 6183–6200.
50. Charalambides PG, Lund J, Evans AG, McMeeking RM. A test specimen for determining the fracture resistance of bimaterial interfaces. *Journal of Applied Mechanics* 1989; **56**:77–82.
51. Suo Z. Singularities, interfaces and cracks in dissimilar anisotropic media. *Proceedings of the Royal Society of London A* 1990; **427**:331–358.